The Astrophysical Journal, 754:9 (9pp), 2012 July 20 doi:10.1088/0004-637X/754/1/9

HARD X-RAY OBSERVATIONS OF A JET AND ACCELERATED ELECTRONS IN THE CORONA

Lindsay Glesener[1], Säm Krucker[2], and R. P. Lin[1,3]
Space Science Laboratory, UC Berkeley, 7 Gauss Way, Berkeley, CA 94720, USA; glesener@ssl.berkeley.edu
Received 2011 December 24; accepted 2012 May 13; published 2012 June 28

ABSTRACT

We report the first hard X-ray observation of a solar jet on the limb with flare footpoints occulted, so that faint emission from accelerated electrons in the corona can be studied in detail. In this event on 2003 August 21, *RHESSI* observed a double coronal hard X-ray source in the pre-impulsive phase at both thermal and nonthermal energies. In the impulsive phase, the first of two hard X-ray bursts consists of a single thermal/nonthermal source coinciding with the lower of the two earlier sources, and the second burst shows an additional nonthermal, elongated source, spatially and temporally coincident with the coronal jet. Analysis of the jet hard X-ray source shows that collisional losses by accelerated electrons can deposit enough energy to generate the jet. The hard X-ray time profile above 20 keV matches that of the accompanying Type III and broadband gyrosynchrotron radio emission, indicating both accelerated electrons escaping outward along the jet path and electrons trapped in the flare loop. The double coronal hard X-ray source, the open field lines indicated by Type III bursts, and the presence of a small post-flare loop are consistent with significant electron acceleration in an interchange reconnection geometry.

Key words: Sun: corona – Sun: flares – Sun: radio radiation – Sun: X-rays, gamma rays

Online-only material: color figures

1. INTRODUCTION

An emerging flux reconnection model of solar flares was first proposed by Heyvaerts et al. (1977) and later expanded upon by Shibata and others (Shibata et al. 1989, 1992b; Yokoyama & Shibata 1996) to include flare-related jets. According to this model (Figure 1), magnetic buoyancy causes magnetic flux to emerge from the chromosphere into the corona, where reconnection occurs between the emerging field and the overlying coronal field. This is referred to as "interchange reconnection" if a field line that is open to interplanetary space switches the location of its photospheric footpoint. This model places the reconnection site in the corona. Post-reconnection field lines take the shape of a small, hot loop and field lines that are open to interplanetary space.

Simulations suggest that a fast shock can arise in regions where the reconnection outflow reaches a strong perpendicular magnetic field. Gas pressure behind this shock could drive a jet along these field lines with a speed on the order of the Alfvén speed. Another jet could arise from chromospheric evaporation; this comparatively cooler jet should have as its characteristic velocity the local sound speed, and could be present concurrently with the former jet (Yokoyama & Shibata 1996).

The soft X-ray jets predicted by this model were first observed by the Soft X-ray Telescope (SXT) aboard *Yohkoh* (Shibata et al. 1992a). Hundreds of jets were observed over *Yohkoh*'s lifetime. Shimojo et al. (1996) performed a statistical study of *Yohkoh* jets, measuring the lengths, lifetimes, and velocities of 100 jets. Apparent velocities were determined to be 10–1000 km s^{-1}, with 200 km s^{-1} the average value.

More recently, Kim et al. (2007) performed a study of three *Hinode* jets with overlapping *Transition Region and Coronal Explorer* (*TRACE*) coverage, finding velocities from 90 to 310 km s^{-1}. *Hinode* observations of the polar coronal holes (Savcheva et al. 2007; Cirtain et al. 2007) have found tens to hundreds of X-ray jets per day, with multiple jet velocity components of ∼200 and ∼800 km s^{-1}. Chifor et al. (2008) determined that a repeated extreme-ultraviolet (EUV)/X-ray jet arose from chromospheric evaporation. Hα surges (Roy 1973) have been found to represent cooler counterparts to many hot X-ray jets (Chae et al. 1999; Jiang et al. 2007).

Jets are strongly correlated with Type III radio bursts (e.g., Raulin et al. 1996) and are sometimes associated with impulsive, electron/^{3}He-rich solar energetic particle (SEP) events observed in the interplanetary medium (Nitta et al. 2008; Wang et al. 2006), indicating that accelerated electrons have access to open field lines. Any accelerated electrons traveling downward would lose their energies to collisions, producing three hard X-ray (HXR) footpoints as shown (dark blue) in the diagram in Figure 1. Krucker et al. (2011b) studied the HXR emission for 16 flares associated with prompt solar impulsive electron events observed at 1 AU to energies above 50 keV and found that 7 of these show three-footpoint configurations consistent with interchange reconnection. Seven of the remaining events show two footpoints (four with an elongated source that may be hiding a third source) and two are unresolved. All six events with *TRACE* coverage show EUV jets with onsets at the time of the HXR emission (within the tens of seconds of cadence). This suggests that prompt impulsive electron events are often instigated by interchange reconnection.

Fainter HXR sources should also exist in the corona along nonthermal electron paths and will be brightest where the density is enhanced, for example, in the vicinity of the hypothesized fast shocks (purple regions, Figure 1). Compared with footpoints, however, coronal sources are expected to be fainter by $\gtrsim$1–2 orders of magnitude, which is at or beyond the dynamic range of current instrumentation. Furthermore, any coronal HXR emission from jets emitted along the observer's line of sight will be difficult to disentangle from footpoint emission. Despite these obstacles, Bain & Fletcher (2009) found an example of HXR emission from a large two-ribbon flare on the disk

[1] Also at Physics Department, University of California at Berkeley, USA.
[2] Also at Institute of 4-D Technologies, School of Engineering, University of Applied Sciences Northwestern Switzerland.
[3] Also at School of Space Research, Kyung Hee University, Republic of Korea.

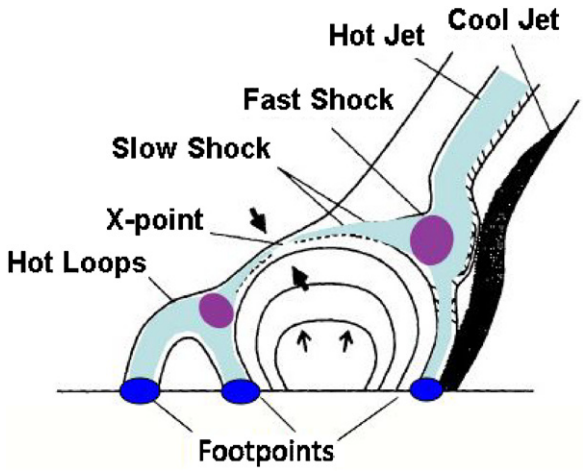

Figure 1. Black: two-dimensional diagram of reconnection as a result of emerging flux according to the Heyvaerts–Shibata model; drawing based on Shibata et al. (1997). Overlaid on this diagram are hypothetical HXR sources (not from the original model), including paths traveled by energetic electrons (light blue), bright HXR footpoints in which electrons lose all energy (dark blue), and dense shock regions where energetic electrons may undergo collisions (purple). With current instrumentation, the coronal sources are unlikely to be seen in the presence of bright footpoints.

(A color version of this figure is available in the online journal.)

that coincided with an EUV jet. HXR and radio data suggested the presence of nonthermal electrons in the jet itself. In summary, several HXR and radio observations have indicated that interchange reconnection is an important driver for solar jets.

Here, we present *Reuven Ramaty High Energy Spectroscopic Imager (RHESSI)* observations of HXR emission from a coronal jet at the limb. The base of the jet (and the accompanying flare) was occulted, so that HXR coronal sources can be studied without the presence of bright footpoint emission. Much of the jet's motion occurs in a direction transverse to the line of sight, so that elements of the two-dimensional model shown in Figure 1 can be clearly seen. We find coronal HXR sources at three distinct times: (1) a double source in the pre-impulsive phase; (2) a near-limb source during the first impulsive burst, coinciding with the lower of the two earlier sources; and (3) an additional, elongated nonthermal source occurring co-temporally and co-spatially with the jet, in the second impulsive burst. This observation is the first to see multiple coronal HXR sources in conjunction with a coronal jet.

2. OBSERVATIONS

The *RHESSI* mission provides high-resolution X-ray spectra and full-disk images of the Sun from 3 keV to 17 MeV (Lin et al. 2002). On 2003 August 21, *RHESSI* observed a flare just over the western solar limb with a pre-impulsive phase and two HXR bursts. This flare began at ∼15:18 UT and was a *GOES* class C4.9 flare (top panel, Figure 2). To find the most likely heliocentric location of the flare, its active region (10431) was tracked across the solar disk using locations of *GOES* X-ray flares (from the *GOES* event database) and *RHESSI* flares (from the *RHESSI* microflare list). Using actual flare locations was necessary in order to isolate the flaring section(s) of this rather large, complex active region. The flare longitudes were plotted versus time and fit with a linear function, which was extrapolated to locations beyond the limb. Uncertainties in the calculated occultation are taken from the uncertainties in the linear fit parameters (caused by variation in the flare locations). The average flaring location of the active region was thus determined to be disk-occulted by 1.6 ± 2.5 deg at the time of this flare. It is therefore likely that the event was occulted by between 0 and 4.1 deg (corresponding to an occultation height of 0 to 1.8 Mm), based on locations of previous flares. The occultation could be even greater if the flare came from a different section of the active region than the one that produced the on-disk flares. Based on this analysis alone, it is impossible to conclude whether the flare was occulted. However, no footpoints are apparent in *RHESSI* X-ray images; only coronal sources are observed (see the discussion at the end of Section 3.1), leading us to conclude that the event was partially occulted.

A small coronal mass ejection (CME) was observed after the flare by the Large Angle and Spectrometric Coronagraph (LASCO) aboard the *Solar and Heliospheric Observatory*. The CME had an angular width of 63 deg and a velocity of 231 km s^{-1}, according to the LASCO CME catalog (Gopalswamy et al. 2009). It is doubtful that the CME was associated with this flare; it is first visible in C2 images at 1554 UT and a constant-velocity projection indicates that the CME left the solar surface before 1400 UT. If the CME underwent significant deceleration, then it could have originated at the time of the flare.

An impulsive non-relativistic electron event was observed near Earth by the *Wind* spacecraft ∼40 minutes after this flare. However, it is likely that this electron event was not associated with this flare but instead with an interplanetary radio burst that took place ∼20 minutes afterward.

2.1. TRACE EUV Observations

The *TRACE* spacecraft (Handy et al. 1999) was observing the limb in the vicinity of the flare. Around 15:20 UT, *TRACE* observed a UV/EUV jet emerging from the region. Figure 3 shows a *TRACE* 171 Å time sequence of the jet, with a pre-jet image from 15:15:02 UT subtracted from each frame. (Note that a gap exists between 15:23:19 UT and 15:26:20 UT.) The base of the jet is not visible in this filter because a filament obscures the near-limb region. The jet begins as an emergence along multiple field lines (times 15:20:39 UT and 15:21:19 UT). As the event proceeds, the brightening develops finer structure, with more northern field lines also brightening (times 15:21:59 UT and 15:22:39 UT). Later, after the events discussed here, the jet becomes stronger and more collimated (last two panels).

In order to measure the jet velocity, the jet height was tracked over time. The *TRACE* 171 Å filter was chosen for this measurement because of its higher cadence (usually 40 s), though the jet cannot be tracked below ∼10 Mm because of the obscuring filament. Using running difference maps, emission was integrated across the width of the jet and the resulting height profile tracked over time. (See Figure 2, bottom panel.) A line was fit to the 50% intensity level for the three most intense time intervals, with the midpoint of the time interval as the independent variable. The jet velocity, given by the slope of this line, is 417 ± 73 km s^{-1}. This is a lower limit since the line-of-sight motion is unknown. The uncertainty was determined by randomly varying the time within each interval and recomputing the slope. The jet is first visible in a 40 s *TRACE* image centered at 15:20:39 UT; extrapolation of the height profile back to the solar limb shows that the jet could have originated up to 47 s earlier than this.

The jet temperature cannot be determined from *TRACE* data because of the lack of simultaneous multiwavelength images. The jet is visible in the 171 Å filter, which is most sensitive

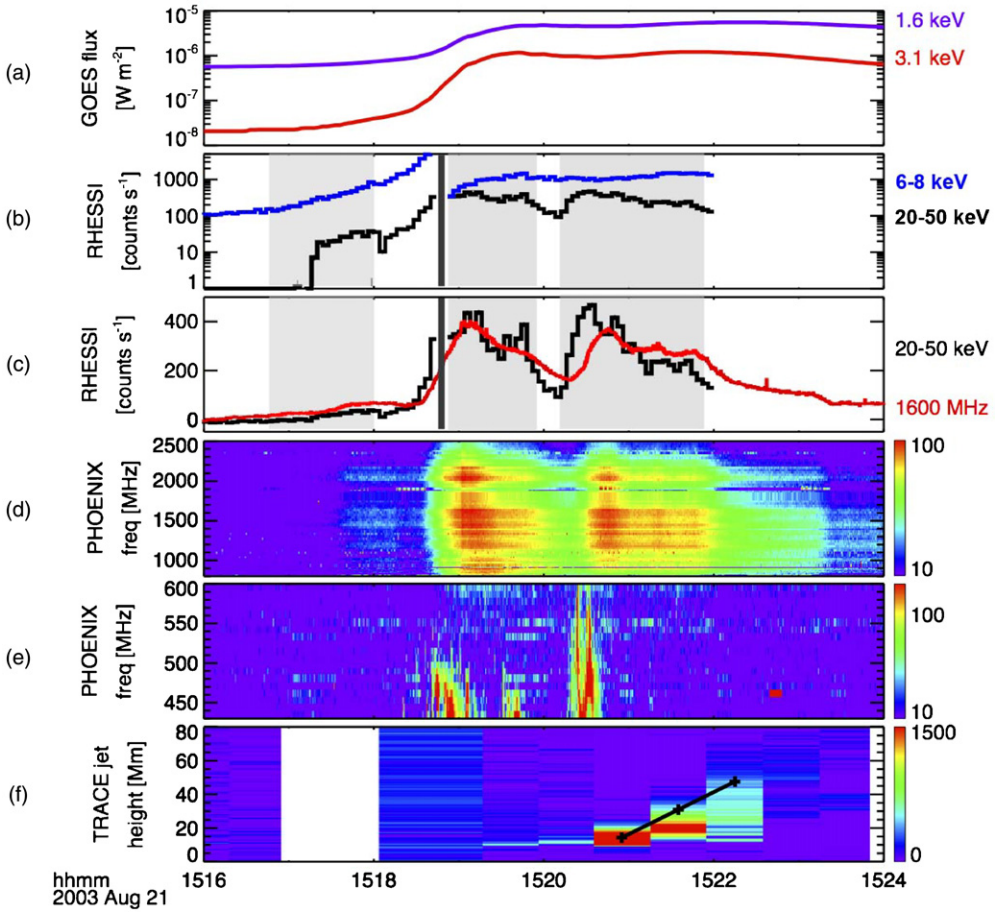

Figure 2. Time profiles of the 2003 August 21 limb event. Panel (a) *GOES* light curves. Panel (b) *RHESSI* 6–8 keV emission (blue) and 20–50 keV emission (black), log scale. Panel (c) *RHESSI* 20–50 keV emission (black) and Phoenix-2 1600 MHz emission (red), linear scale. Panel (d) Phoenix-2 decimetric bursts. Panel (e) Phoenix-2 Type III bursts. Panel (f) *TRACE* 171 Å jet height profile, in Mm above the optical limb. There is a gap in the *TRACE* data before 1518 UT. The jet velocity is the slope of the solid black line fit to three time intervals. In panels (b) and (c), the black bar marks the attenuator motion, while gray shading indicates the image times.

(A color version of this figure is available in the online journal.)

to plasma of ∼1 MK but also has a smaller sensitivity peak at 10 MK (Phillips et al. 2005). Jets are commonly observed across a wide frequency range, being simultaneously observed in UV, EUV, and X-ray images (Alexander & Fletcher 1999; Kim et al. 2007), suggesting a multithermal nature.

2.2. *RHESSI* HXR Observations

For the 2003 August 21 event, *RHESSI* observed a pre-impulsive phase (15:16:44–15:18:01 UT) and two X-ray bursts (15:18:53–15:19:49 UT and 15:20:18–15:21:55 UT) (Figure 2), before the spacecraft entered the South Atlantic Anomaly. Figure 4 shows *RHESSI* images and spectra from three time intervals, overlaid on a *TRACE* 1550 Å image at 15:23:35 UT that shows the UV jet. Although none of the *RHESSI* images occur simultaneously with this image (*RHESSI* images are from 2 to 7 minutes earlier), the overall geometry can be studied. *RHESSI* images were produced using the maximum entropy method (MEM) imaging technique (Schmahl et al. 2007); all images were checked for consistency with CLEAN images. The images were co-aligned by adjusting the *TRACE* roll angle until a *TRACE* 195 Å image matched an image from the EIT telescope. The co-alignment of the *TRACE* and *RHESSI* images is expected to be good to 5 arcsec.

A summary of source parameters for all three time periods is presented in Table 1.

2.2.1. Pre-impulsive Phase: Double Coronal Source

Panel (a) in Figure 4 shows *RHESSI* thermal (red) and nonthermal (blue) sources during the pre-impulsive phase (15:16:44–15:18:01 UT), before the attenuator insertion. Two coronal sources are visible: a source near the limb and a high coronal source ∼10 arcsec above the limb, both emitting at thermal and nonthermal energies. This time period is 2–4 minutes before the EUV jet first appears.

Panel (d) shows a spatially integrated HXR spectrum during this time interval. Due to low statistics, detailed imaging spectroscopy cannot be performed. However, fluxes in each source were compared in two energy bands (10–15 and 15–25 keV) to obtain approximate spectral exponents for assumed power-law distributions, with the result that the high-altitude source shows a softer spectrum (Table 1). Assuming a cutoff energy of 16 keV for each, the energy deposited for both thin- and thick-target models was calculated, using formulas in Lin (1974), and was found to be on the order of 10^{27}–10^{28} erg, respectively.

2.2.2. First HXR Burst: Near-limb Source

The image shown in panel (b) of Figure 4 covers the first nonthermal burst of the flare from 15:18:53 UT to 15:19:49 UT, with a primary peak at 15:19:10 UT and a secondary peak at 15:19:45 UT. The higher coronal source detected in the

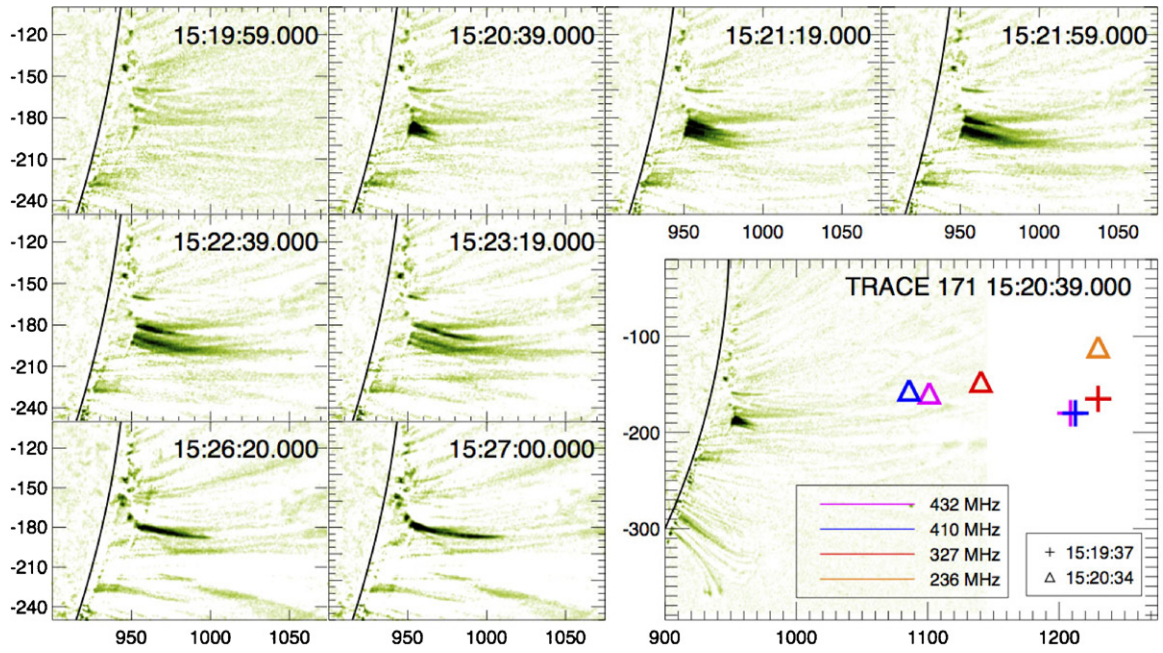

Figure 3. *TRACE* 171 Å images of the 2003 August 21 jet, with a pre-event image at time 15:15:02 UT subtracted. The first six frames show emission that is concurrent with the X-ray and radio observations; the last two frames show the beginning of the next jet. There is a gap in the 171 Å data between 15:23:19 UT and 15:26:20 UT. A filament obscures the jet near the limb in this filter; it is in this region that the HXR sources discussed in Section 2.2 lie. The bottom-right image shows the start of the EUV jet overlaid with source locations from the Nançay Radioheliograph (NRH); these data are discussed in Section 2.3. Markers indicate NRH source centroids at the time of the second (plus signs) and third (triangles) Type III bursts, around 15:19:37 UT and 15:20:34 UT, respectively.

(A color version of this figure is available in the online journal.)

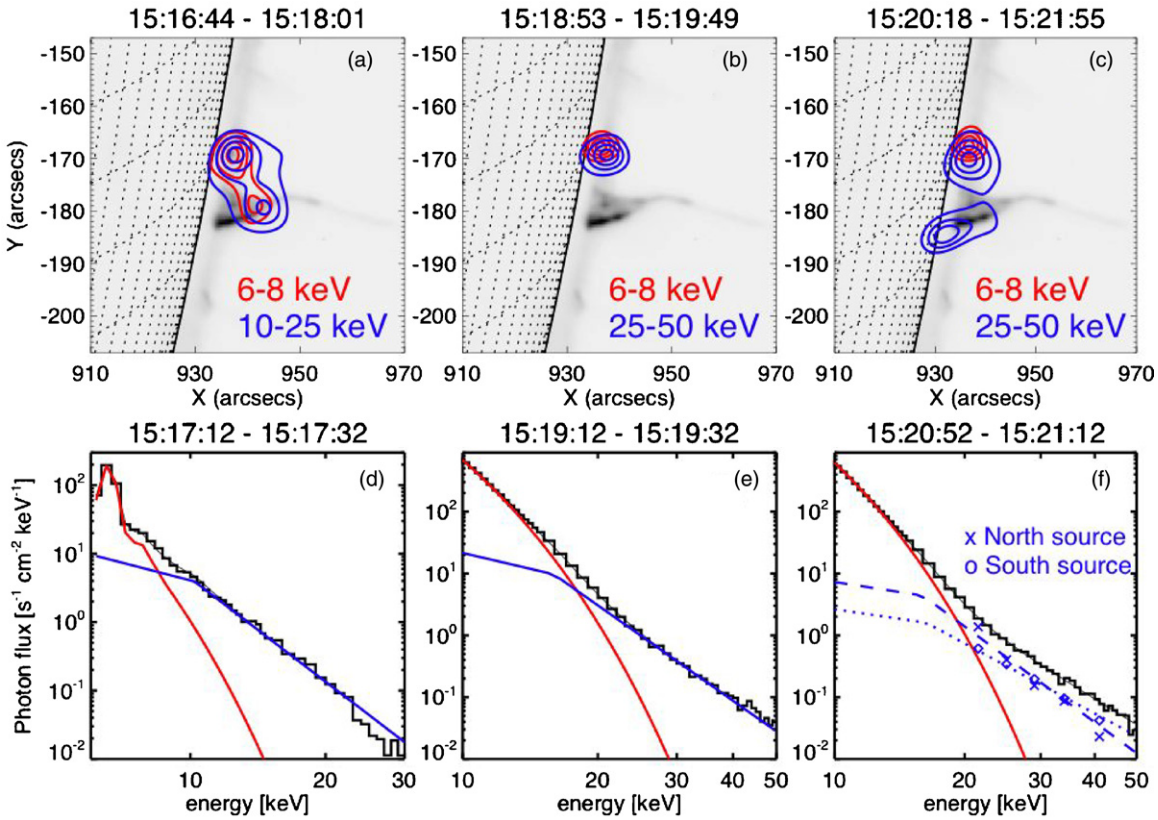

Figure 4. *RHESSI* X-ray images and spectra of the 2003 August 21 flare, during the pre-impulsive phase (left column), the first nonthermal burst (middle column), and the second nonthermal burst (right column). Top row: thermal contours (red) and nonthermal contours (blue) superimposed on a later *TRACE* 1550 Å image of the jet. The *TRACE* image time is 15:23:35 UT in all images. Bottom row: *RHESSI* spectra, assuming a spectral index of 1.7 below the break. In panel (f), the spectrum was fit with two broken power laws (dashed lines) to represent the two nonthermal sources. All *RHESSI* images were produced using the MEM_NJIT imaging algorithm with subcollimators 3–9. Contour levels are 30%, 50%, 70%, and 90%.

(A color version of this figure is available in the online journal.)

Table 1
Spectral Parameters of the *RHESSI* X-Ray Sources

Time	Location	Area[a]	T (MK)	EM (cm^{-3})	n (cm^{-3})	γ	ϵ_0 (keV)[b]	E_{thin} (erg)[c]	E_{thick} (erg)[d]
Pre-impulsive phase (15:16:44–15:18:01)	Near-limb	$6'' \times 8''$	13[e]	6.7×10^{46}[e]		2.7–4.2	16[e]	$5–9 \times 10^{26}$	$1–4 \times 10^{27}$
	High-altitude	$3'' \times 4''$				4.4–5.2	16[e]	$1–2 \times 10^{27}$	$5–9 \times 10^{27}$
First HXR burst (15:18:53–15:19:49)	Near-limb	$5'' \times 4''$	24	8.5×10^{47}	1.6×10^{11}	5.1	16	1×10^{29}	7×10^{29}
Second HXR burst (15:20:18–15:21:55)	Near-limb north	$5'' \times 5''$	22	1.1×10^{48}	1.5×10^{11}	5.7	16	5×10^{28}	3×10^{29}
	Near-limb south (jet)[f]	$8'' \times 4''$				3.8	16	1×10^{28}	4×10^{28}

Notes.
[a] Areas are taken from MEM images of thermal sources, except for the last source. Since no thermal source is seen from the jet location the nonthermal source area is listed instead.
[b] Break energy of the photon spectrum.
[c] Energy deposited in ambient plasma in a thin-target regime.
[d] Energy deposited in ambient plasma in a thick-target regime.
[e] The low count rates in this time interval do not allow for detailed imaging spectroscopy of the individual sources. The temperature and emission measure given here are from the integrated spectrum, not individual sources. Spectral indices are estimated from comparison of flux measured in two energy bands, and a cutoff energy of 16 keV is assumed for the computation of deposited energy.
[f] There is no observable thermal emission from the jet X-ray source. See Section 3.2 for discussion.

pre-impulsive phase is no longer detectable, possibly due to dynamic range limitations, since the remaining, near-limb source is about two orders of magnitude more intense than the pre-impulsive phase sources. The near-limb source has both a hot (24 MK) thermal component and a nonthermal component significantly steeper ($\gamma = 5.1$) than in the pre-impulsive phase (Figure 4, panel (e); Table 1). The centroids of the thermal and nonthermal sources differ by ~2 arcsec. (Centroids were obtained using vis_fwdfit, a visibility-based forward-fitting imaging routine; see, e.g., Dennis & Pernak 2009.)

2.2.3. Second HXR Burst: X-Ray Emission from the EUV Jet

Panel (c) of Figure 4 shows an X-ray image at the time of the second nonthermal burst, from 15:20:18 to 15:21:55 UT. The northern, near-limb coronal source is still visible, but now a new, elongated, southern source appears. Comparison with the UV background image shows that this source originates from the location of the *TRACE* jet, and the HXR burst occurs at the same time as the jet (see Figure 2), indicating that the HXR originate from the jet itself. The jet is not seen in thermal X-rays (~6–10 keV), possibly due to dynamic range limitations since the northern thermal source is very bright. (See discussion in Section 3.2.)

Since this HXR image contains two spatially distinct sources, a nonthermal spectrum was computed for each source individually using imaging spectroscopy, as in Krucker & Lin (2002), and two power-law indices were obtained. To obtain cutoff energies and thermal parameters, these results were then used as initial parameters to fit the integrated spectrum with one thermal component and two broken power laws to represent the separate nonthermal sources. These spectra are shown in panel (f) of Figure 4 and parameters are given in Table 1. The northern source is at the same location as the near-limb source of the first HXR burst, with similar thermal (22 MK) and nonthermal ($\gamma = 5.7$) components. The southern nonthermal jet source is weaker but has a significantly harder spectrum ($\gamma = 3.8$). Its elongated shape points toward the high coronal source of the pre-impulsive phase.

2.3. Radio Observations

Radio emission from the August 21 event was observed by the Phoenix-2 solar radio spectrometer in Bleien, Switzerland, which records in frequencies from 0.1 to 4 GHz (Messmer et al. 1999; Figure 2, panels (d) and (e)). Type III radio bursts occur in three bunches, while gyrosynchrotron bursts occur at higher frequencies. Together, these two components produce radio emission that closely mimics the *RHESSI* HXR profile above ~20 keV. The first two Type III bursts start at ~500 MHz and coincide with the primary and secondary peaks of the first HXR burst, respectively. The third Type III burst starts at $\gtrsim$600 MHz, simultaneous with the peak of the second HXR burst. These are followed by longer bursts of gyrosynchrotron emission that coincide with the duration of each HXR burst (Figure 2, panel (c)).

The Nançay Radioheliograph (NRH; Kerdraon & Delouis 1997) provides images at 432, 410, 327, and 236 MHz. The source locations at the time of the last two Type III bursts are shown in Figure 3, overlaid on a *TRACE* image of the beginning jet. The radio sources are located higher with decreasing frequency, characteristic of electron beams moving radially outward through progressively less dense plasma. The field lines along which the jet emerges point toward the NRH sources, suggesting that the jet takes the same path as the Type III-generating electron beams. Raulin et al. (1996) also found that solar jets and Type III-emitting electrons follow similar paths. Compared with the second burst, the path of the last burst is translated to the north by ~50 arcsec. As discussed in Section 2.1, the jet displays the same behavior.

Christe et al. (2008) studied an unusual series of six Type III bursts, each simultaneous with an HXR microflare, but found that the HXRs were thermal, not nonthermal bremsstrahlung from the Type III-emitting electron beams. Krucker et al. (2008b) found a partially occulted event in which the nonthermal HXR and Type III emission were temporally correlated. In the event presented here, the HXR emission appears to be temporally correlated with the combined Type III and gyrosynchrotron emission. (See Figure 2, panel (c).)

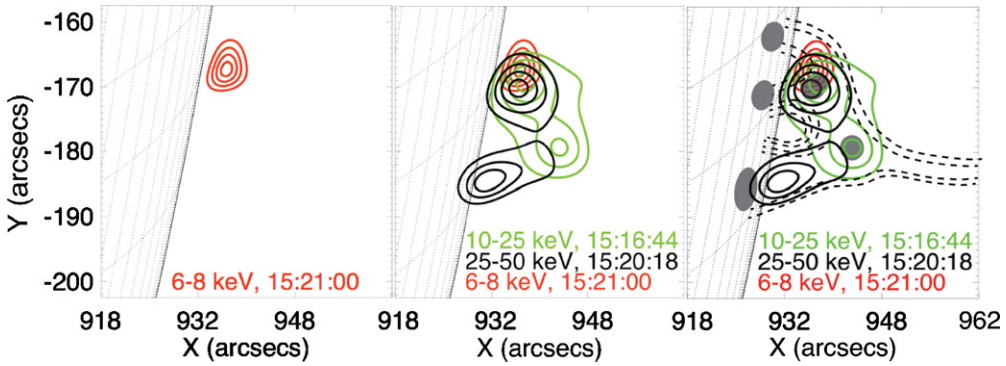

Figure 5. Left: *RHESSI* thermal emission from a small post-flare loop in the latter half of the second HXR burst (red). Middle: overlays of *RHESSI* nonthermal emission from the pre-impulsive phase reconnection outflow (green) and the jet emission (black). Reconnection outflow is correctly positioned to supply energetic electrons to the post-flare loop. Right: these sources are overlaid on a cartoon of interchange reconnection similar to that in Figure 1, demonstrating the expected locations of HXR sources.

(A color version of this figure is available in the online journal.)

3. DISCUSSION

3.1. Evidence for Interchange Reconnection

In the right-hand panel of Figure 5, a diagram of the Heyvaerts/Shibata model is shown with the observed X-ray sources overplotted. The pre-impulsive double source (shown in green, middle and right panels) appears to correspond to the locations of the hypothesized fast shocks formed by reconnection outflow. One outflow jet is aimed downward toward the limb and the other is projected laterally, higher in the corona. The nonthermal HXR emission in the corona indicates the presence of accelerated electrons up to >30 keV. This is consistent with the reconnection and acceleration regions being located between the two coronal sources. Studies of flares on 2002 April 15 (Sui & Holman 2003), 2002 April 30 (Liu et al. 2008), and 2003 November 3 (Chen & Petrosian 2012) also found double sources in the corona and in each case inferred a reconnection site between the two sources. Pre-impulsive thermal and nonthermal HXR emission was also detected in the corona in the 2002 July 23 X4.3 flare, and attributed to the reconnection process (Caspi & Lin 2010).

In the first intense HXR burst (∼15:19 UT), the emission from the near-limb source becomes brighter by two orders of magnitude. A high-corona source could still be present, as in the pre-impulsive phase, but only if it is $\gtrsim$10 times fainter than the near-limb source, in order to be undetected. Two Type III radio bursts are observed simultaneously with the primary and secondary peaks of the HXR burst. This indicates accelerated electrons escaping on open field lines and is consistent with interchange reconnection. Longer-duration broadband gyrosynchrotron emission mimics the time profile of the HXR above 20 keV, suggesting the presence of trapped electrons in a post-reconnection loop.

The second impulsive HXR burst (∼15:21 UT) is coincident with a third type III radio burst that extends up to 600 MHz and occurs close to the onset of the jet, along with another long burst of gyrosynchrotron emission. A new HXR source shown in black contours in Figure 5, middle and right panels) is spatially coincident with and elongated along the jet, pointing toward the high coronal source observed in the pre-impulsive phase. Scenarios for producing HXR from the jet will be discussed in the next section.

The jet velocity of 417 ± 73 km s^{-1} is faster than most of the *Yohkoh* jets studied by Shimojo et al. (1996; average 200 km s^{-1}) and the *Hinode* jets studied by Kim et al. (2007; 90–310 km s^{-1}). Bain & Fletcher (2009) found a similar velocity (∼500 km s^{-1}) for a *TRACE* jet which also showed *RHESSI* nonthermal HXR emission. The velocity is on the order of the Alfvén speed, for example for a coronal density of ∼10^{10} cm^{-3} and a magnetic field of ∼20 G. However, the velocity is also consistent with the local sound speed for temperatures of ∼12 MK. (Possible temperatures will be considered in the next section.) Therefore, the jet cannot be distinguished by its velocity as either Shibata's "hot" (gas pressure) or "cool" (chromospheric evaporation) jet. However, in the *TRACE* 1550 Å filter (see panel (a) of Figure 4), the jet is visible below the higher coronal HXR source, suggesting a chromospheric or low coronal origin.

Late in the event (in the latter half of the second HXR burst), the northern thermal source becomes elongated parallel to the limb (left panel, Figure 5). This is consistent with the heating and filling of a small post-reconnection loop at the far northern side of the flare, as predicted by the Heyvaerts/Shibata model. Comparison with the earlier double coronal sources (Figure 5, middle and right panels, green contours) confirms that this loop is in the correct location for energized electrons from the reconnection region to be injected into it.

One other magnetic geometry for this flare was considered: that of the standard flare model, in which electrons accelerated in the corona are injected radially downward into a single flare loop and stream down the loop legs until they reach chromospheric footpoints. In this geometry the three observed HXR sources would correspond to a looptop (or above-the-looptop) source and two footpoints. However, the near-limb HXR source locations, timing, and spectra are inconsistent with flare footpoints. The northern source displays thermal emission slightly below the nonthermal source (see panel (b) of Figure 4), while for a flare footpoint higher-energy emission should be located at lower altitudes. The 6–8 keV emission observed late in the event from the northern source (see Figure 5, left panel) is indicative of a thermal post-flare loop, not a footpoint, which should emit primarily at nonthermal energies and which should be closer to the limb. The southern source (see panel (c) of Figure 4) starts at the limb but is too elongated (8 arcsec) to be a footpoint. Furthermore, the timing of the near-limb sources, in which the northern source appears 2–4 minutes before the southern source, is inconsistent with a looptop injection followed by precipitation in the two footpoints, which would result in a high coronal source appearing just before,

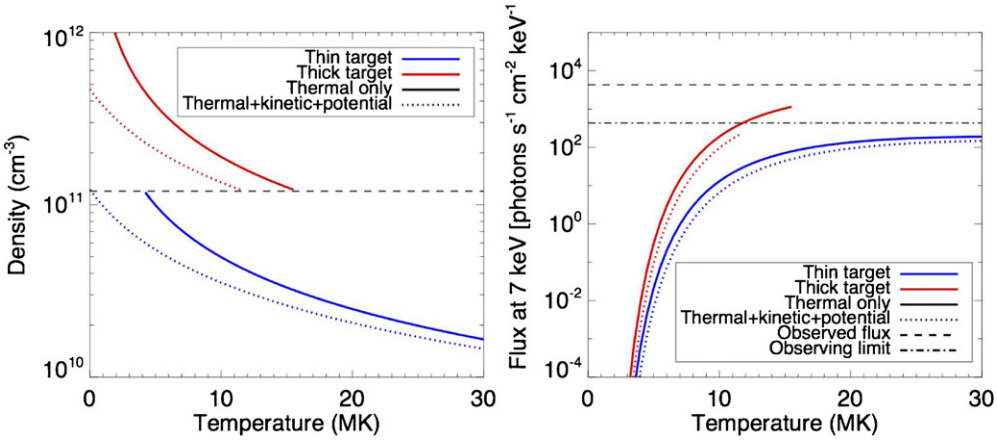

Figure 6. Left: the relation between the jet density and temperature in the thin- and thick-target approximations, assuming all energy deposited in the nonthermal source is transferred into thermal energy of the jet (solid lines) or allowing for additional loss to jet kinetic and potential energies (dotted lines). The dashed black line indicates the density (1.2×10^{11} cm^{-3}) separating the two regimes. Right: simulated flux at 7 keV for a range of temperatures, with densities taken from the left panel. Only values from the left panel are included in the plot. The dashed line marks the flux observed from the bright northern source, while the dash-dotted line marks a conservative observing limit of 10 times fainter. Fluxes below the dash-dotted line probably could not be seen within *RHESSI*'s dynamic range.

(A color version of this figure is available in the online journal.)

or simultaneously with, the footpoints. When the two near-limb sources are observed together (in the last time interval) their spectral indices differ by 1.9. Saint-Hilaire et al. (2008) studied 53 on-disk flare footpoint pairs and found that none had a difference in spectral index of >0.8. The simple loop model is thus ruled out for this flare.

3.2. HXR Emission from the Jet

HXRs from the jet itself could be produced by accelerated electrons traveling either upward or downward through the source, which could be approximated as either a thin or thick target for energetic electrons. Here, we will consider both regimes and first assume the electrons are traveling downward toward the chromosphere.

3.2.1. Thick-target HXR Emission from the Jet

If electrons are accelerated in the corona, travel downward, and lose all their energy in the jet source, then the jet HXR emission can be considered a coronal thick target. In this scenario the electrons never reach the chromosphere. Coronal thick-target emission, while extremely rare, is occasionally observed (Veronig & Brown 2004). With the observed HXR source parameters (photon spectral index $\gamma \sim 3.8$, cutoff energy ~16 keV, and length ~8 arcsec), the average electron energy is ~22 keV. The column density necessary to stop a beam of energetic electrons is $N = 1.5 \times 10^{17}$ cm^{-2} $(E/\mathrm{keV})^2$ (Krucker et al. 2008a), so the ambient density averaged over the source must be $>1.2 \times 10^{11}$ cm^{-3}. The energy deposited by accelerated electrons in a thick-target jet volume is 4×10^{28} erg (see Table 1, lower-right cell).

Can energetic electrons deposit enough energy in this thick target source to supply the energy necessary for the jet? A cylinder with dimensions of the jet HXR source (8″ by 4″) has a volume of 5×10^{25} cm^3. The average density is $>1.2 \times 10^{11}$ cm^{-3} (for a thick target), so the total number of atoms is $>6 \times 10^{36}$. The jet is visible at least up to 50 Mm and the measured jet velocity is 417 km s^{-1}, so the kinetic and gravitational potential energies are $\gtrsim 8 \times 10^{27}$ and $\gtrsim 1 \times 10^{27}$ erg, respectively, using the proton mass for each atom. The total jet energy is thus $\gtrsim 1 \times 10^{28}$ erg, which is less than the energy deposited by accelerated electrons in the jet volume.

The difference between the deposited energy and the jet kinetic and potential energies goes into heating of the jet, neglecting any energy escaping downward. The jet's temperature cannot be measured from observations by either *TRACE* (no overlapping multiwavelength images) or *RHESSI* (no observed thermal source), but constraints can be obtained. The thermal energy is $U = 3k_B T n V$, where k_B is Boltzmann's constant and U, n, T, and V are the jet's thermal energy, density, temperature, and volume, so the jet density and temperature are related by $nT = U/(3k_B V)$. If *all* the energy deposited by nonthermal electrons goes into thermal heating, then $nT \approx 2 \times 10^{18}$ K cm^{-3}; this relation is shown in the left panel of Figure 6 (solid red line). If a portion of the energy goes into jet kinetic and potential energy, as discussed above, then the relation is modified (dotted red line). The necessary density for a thick-target approximation ($>1.2 \times 10^{11}$ cm^{-3}) thus allows a range of temperatures below ~12 MK (according to the dotted red line).

This constraint is confirmed by the lack of a *RHESSI* thermal source. The jet travels on field lines open to interplanetary space, so it is possible that plasma does not remain in the region long enough to be heated to a high enough temperature to be observed. Thermal sources detected by *RHESSI* are usually found in closed loops. Moreover, if a thermal source at the location of the jet is $\gtrsim$10 times fainter than the bright northern source, it might not be detectable within *RHESSI*'s dynamic range. In the right panel of Figure 6, soft X-ray fluxes at 7 keV are calculated for a range of temperatures (solid and dotted red lines) and compared with the observed flux from the northern source (dashed line) and the estimated observing limit (dash-dotted line). It can be seen that a jet thermal source with temperature below ~11–15 MK likely would not be detected within the dynamic range of the instrument.

3.2.2. Thin-target HXR Emission from the Jet

For jet densities lower than $\sim 10^{11}$ cm^{-3}, the downward-traveling energetic electrons would not lose all their energy in the HXR source. In this case the electrons pass through the region and instead deposit most of their energy in an occulted chromospheric footpoint (the southernmost gray footpoint shown in the right panel of Figure 5). Then the energy deposited in the jet HXR source is given by the thin-target formula (Lin 1974).

Compared with the thick-target model, thin-target energy deposition for a given photon spectrum is reduced by a factor of γ, in this case to 1×10^{28} erg (see Table 1). In this scenario the electrons deposit most of their energy in an unseen footpoint below; the jet thus originates from the chromosphere (through chromospheric evaporation by the accelerated electrons) and is only further heated in the corona. In this scenario the HXR-producing energetic electrons will still collisionally deposit enough energy to generate the jet, but now this occurs in the unseen footpoint.

The thin-target density–temperature relation is plotted in blue in the left panel of Figure 6; estimated flux at 7 keV is plotted in blue in the right panel. None of the allowed density–temperature pairs would produce a thermal source observable by *RHESSI*. However, this calculation neglects heating by energetic electrons in the chromosphere, which would presumably heat the evaporating plasma before it emerges into the corona. Fisher et al. (1984) showed that at least half the energy of evaporating material is thermal and that velocities of a few times the sound speed can be attained, so that the jet should be heated to >2 MK before reaching the corona if it is produced by chromospheric evaporation.

In either the thick- or thin-target scenarios it is clear that the HXR-producing energetic electrons can collisionally deposit enough energy to generate the jet. It is unclear why a jet is generated in the second, but not the first, impulsive HXR burst. Comparison of the more northern source in the two bursts indicates that the first burst exhibited twice as much energy deposition as the second burst (see Table 1) and thus presumably contained enough energy to generate a jet. A possible explanation is that the reconnection process is not symmetric, and so the northern source is not a good point of comparison for the two bursts. It is also possible that there is a time lag between the energy deposition and the jet emergence, so that it is the first burst that generates the jet. (The precise jet start time cannot be derived from *TRACE* observations; also, if the jet initially accelerated then the start time would be earlier than that obtained from the linear extrapolation indicated in Figure 2.) In this scenario, the downward-traveling accelerated electrons only become detectable in HXRs when the high-density jet is present. An extended injection or coronal trapping would be necessary so that the first energetic electrons to reach the chromosphere generate the jet, while later energetic electrons interact with the emerging jet and produce HXR.

3.2.3. Upward-traveling Electron Beams

An alternative interpretation to those just presented is that the jet HXR source is produced by upward-moving nonthermal electrons. These electrons must be accelerated in the base of the jet and travel upward along the jet path. Fletcher & Hudson (2008) proposed a flare model in which energy is transported from the reconnection site to footpoints by Alfvén waves, not particle beams, and reviewed various mechanisms for acceleration in the footpoints. In this case the role of the double coronal source, which indicates pre-impulsive electron acceleration in the corona, would need to be explained. The jet and accelerated electrons can emerge simultaneously, agreeing well with the timing of the EUV and HXR observations.

If the jet HXR source could be split into a lower and an upper source, the beam direction could be determined by comparing the spectral indices of the two sources. For a downward-traveling beam, the lower part of the source would have a harder spectrum since collisions preferentially deplete lower-energy electrons from the beam. Conversely, for an upward-traveling beam, the upper part of the source would have the harder spectrum. Alternatively, the direction of the beam could be determined by comparing source locations at different energies; Saint-Hilaire et al. (2010) showed that the HXR source height decreases with energy only for electron beams traveling downward into the chromosphere (encountering a positive density gradient). Statistics in this event do not allow us to distinguish between these cases.

4. SUMMARY

The observation presented here is the first to see several HXR coronal sources in an interchange reconnection type jet event. Key aspects include the following:

1. A double coronal HXR source at both thermal and nonthermal energies in the flare pre-impulsive phase, indicating early electron acceleration to tens of keV and heating to 13 MK even before the impulsive flare. These sources may indicate locations of reconnection outflows in the Shibata model.
2. Nonthermal HXR emission spatially and temporally coincident with the EUV jet. Energy deposition by nonthermal electrons is sufficient to provide the thermal, kinetic, and potential energies of the jet.
3. Two intense HXR bursts in the impulsive phase, accompanied by radio emission that closely follows the time profile of *RHESSI* HXR above 20 keV. This includes Type III-emitting beams (suggestive of interchange reconnection) that travel similar paths to that taken by the EUV jet, and gyrosynchrotron emission from electrons trapped in flare loops.
4. A small post-flare loop in the correct position to be heated by energetic electrons from the reconnection region.

To detect weak coronal sources in the presence of stronger sources, instruments with higher sensitivity and dynamic range are needed. Focusing optics such as those soon to be tested on the *FOXSI* rocket (Krucker et al. 2011a) or those included on the astronomy telescope *NuSTAR* (Harrison et al. 2010) could be used to observe HXR components, while The Atmospheric Imaging Assembly aboard the *Solar Dynamics Observatory* (Lemen et al. 2012) can provide density and temperature estimates of the EUV jets. In addition, images from the proposed *Frequency Agile Solar Radiotelescope* (Bastian 2003) could study Type III-emitting electron beams and could provide local density information.

This work was supported by the *RHESSI* project, NASA contract NAS598033. L. Glesener was also supported in part by NASA GSRP grant NNX09AM40H. R.P. Lin was also supported in part by the WCU grant (no. R31-10016) funded by the Korean Ministry of Education, Science and Technology. The authors thank the Observatoire de Paris for providing Nançay data, ETH and FHNW for data from the Phoenix Radio Spectrometer, and the *RHESSI* and *TRACE* teams. The authors would also like to thank the referee for insightful questions.

REFERENCES

Alexander, D., & Fletcher, L. 1999, Sol. Phys., 190, 167
Bain, H. M., & Fletcher, L. 2009, A&A, 508, 1443
Bastian, T. S. 2003, Adv. Space Res., 32, 2705
Caspi, A., & Lin, R. P. 2010, ApJ, 725, L161
Chae, J., Qiu, J., Wang, H., & Goode, P. R. 1999, ApJ, 513, L75
Chen, Q., & Petrosian, V. 2012, ApJ, 748, 33

Chifor, C., Isobe, H., Mason, H. E., et al. 2008, A&A, 491, 279
Christe, S., Krucker, S., & Lin, R. P. 2008, ApJ, 680, L149
Cirtain, J. W., et al. 2007, Science, 318, 1580
Dennis, B. R., & Pernak, R. L. 2009, ApJ, 698, 2131
Fisher, G. H., Canfield, R. C., & McClymont, A. N. 1984, ApJ, 281, L79
Fletcher, L., & Hudson, H. S. 2008, ApJ, 675, 1645
Gopalswamy, N., Yashiro, S., Michalek, G., et al. 2009, Earth Moon Planets, 104, 295
Handy, B. N., Acton, L. W., Kankelborg, C. C., et al. 1999, Sol. Phys., 187, 229
Harrison, F. A., Boggs, S., Christensen, F., et al. 2010, Proc. SPIE, 7732, 77320S
Heyvaerts, J., Priest, E. R., & Rust, D. M. 1977, ApJ, 216, 123
Jiang, Y. C., Chen, H. D., Li, K. J., Shen, Y. D., & Yang, L. H. 2007, A&A, 469, 331
Kerdraon, A., & Delouis, J.-M. 1997, Coronal Physics from Radio and Space Observations, Lecture Notes in Physics, 483, ed. G. Trottet (Berlin: Springer), 192
Kim, Y.-H., Moon, Y.-J., Park, Y.-D., et al. 2007, PASJ, 59, 763
Krucker, S., Battaglia, M., Cargill, P. J., et al. 2008a, A&AR, 16, 155
Krucker, S., Christe, S., Glesener, L., et al. 2011a, Proc. SPIE, 8147, 814705
Krucker, S., Kontar, E. P., Christe, S., Glesener, L., & Lin, R. P. 2011b, ApJ, 742, 82
Krucker, S., & Lin, R. P. 2002, Sol. Phys., 210, 229
Krucker, S., Saint-Hilaire, P., Christe, S., et al. 2008b, ApJ, 681, 644
Lemen, J. R., Title, A. M., Akin, D. J., et al. 2012, Sol. Phys., 275, 17
Lin, R. P. 1974, Space Sci. Rev., 16, 189
Lin, R. P., Dennis, B. R., Hurford, G. J., et al. 2002, Sol. Phys., 210, 3
Liu, W., Petrosian, V., Dennis, B. R., & Jiang, Y. W. 2008, ApJ, 676, 704
Messmer, P., Benz, A. O., & Monstein, C. 1999, Sol. Phys., 187, 335
Nitta, N. V., Mason, G. M., Wiedenbeck, M. E., et al. 2008, ApJ, 675, L125
Phillips, K. J. H., Chifor, C., & Landi, E. 2005, ApJ, 626, 1110
Raulin, J. P., Kundu, M. R., Hudson, H. S., Nitta, N., & Raoult, A. 1996, A&A, 306, 299
Roy, J. R. 1973, Sol. Phys., 28, 95
Saint-Hilaire, P., Krucker, S., & Lin, R. P. 2008, Sol. Phys., 250, 53
Saint-Hilaire, P., Krucker, S., & Lin, R. P. 2010, ApJ, 721, 1933
Savcheva, A., Cirtain, J., Deluca, E. E., et al. 2007, PASJ, 59, 771
Schmahl, E. J., Pernak, R. L., Hurford, G. J., Lee, J., & Bong, S. 2007, Sol. Phys., 240, 241
Shibata, K., Ishido, Y., Acton, L. W., et al. 1992a, PASJ, 44, L173
Shibata, K., Nozawa, S., & Matsumoto, R. 1992b, PASJ, 44, 265
Shibata, K., Shimojo, M., Yokoyama, T., & Ohyama, M. 1997, in ASP Conf. Ser. 111, Magnetic Reconnection in the Solar Atmosphere, ed. R. D. Bentley & J. T. Mariska (San Francisco, CA: ASP), 29
Shibata, K., Tajima, T., Steinolfson, R. S., & Matsumoto, R. 1989, ApJ, 345, 584
Shimojo, M., Hashimoto, S., Shibata, K., et al. 1996, PASJ, 48, 123
Sui, L., & Holman, G. D. 2003, ApJ, 596, L251
Veronig, A. M., & Brown, J. C. 2004, ApJ, 603, L117
Wang, Y.-M., Pick, M., & Mason, G. M. 2006, ApJ, 639, 495
Yokoyama, T., & Shibata, K. 1996, PASJ, 48, 353